Surface wave propagation of thin liquid films on a rotating and nonrotating disk

Lin Wu

Department of Mechanical Engineering, University of Nebraska-Lincoln, Lincoln, Nebraska 68588, USA
(Received 26 July 2004; revised manuscript received 19 April 2005; published 29 July 2005)

We theoretically and numerically study the evolution of axisymmetrical surface waves of a wetting liquid film on a rotating or nonrotating disk. Shock waves may form and propagate driven by the centrifugal and external shearing forces. Surface tension and disjoining pressure due to van der Waals force provide diffusion to the system and smear the surface waves. Multiple waves of a molecularly thin liquid film are merged by the disjoining pressure. Surface waves are planarized by the centrifugal force, surface tension, external shearing force and disjoining pressure.

I. INTRODUCTION

A thin liquid layer flows on the surface of a rotating disk in many scientific and industrial applications. Two of the examples are the spin coating process and the lubrication of magnetic disk surfaces in a modern hard disk drive.

The spin coating technique has been widely used to coat uniform films (for example photoresists) on substrates. In the spin coating process, a liquid droplet is placed at the center of a rotating disk. The droplet spreads outwards driven by the centrifugal spinning and its profile becomes increasingly flat. Eventually a thin film of uniform thickness is left on the disk surface. The fluid dynamics aspects of the spin coating problem have received wide attentions due to its importance and significant literatures already exist [1–12]. Emslie *et al.* formulated the first hydrodynamic theory to study the rate of liquid film thinning of a Newtonian flow on a smooth disk under the action of centrifugal and viscous shear forces [1]. Non-Newtonian theories were developed for more complicated polymer systems by Acrivos *et al.* [2] and Flack *et al.* [3]. The effect of evaporation of solvent was taken into account by Meyerhofer [4]. Yanagisawa analyzed the velocity slippage effect at the disk surface [5]. Middleman [6], Rehg and Higgins [7] considered the effect of external air shearing. The planarization of uneven substrate topography by spin coating has been studied by Stillwagon and Larson [8,9]. Troian *et al.* theoretically [10] and Fraysse and Homsey experimentally [11] identified a fingering instability at the expanding front of the liquid region. More information about the spin coating and other thin liquid film flow phenomena is available in the review article [12].

In modern hard disk drives, a molecularly thin lubricant layer is coated on the rotating magnetic disk to provide the necessary lubrication and protection to the disk surface [13]. Kim *et al.* studied the lubricant depletion phenomenon by considering the effects of physical parameters such as the disk surface roughness, surface tension and disjoining pressure [14].

Due to different sources of disturbance, surface undulations of a liquid film on a rotating disk are unavoidable. Under the action of viscous force, centrifugal force, external shearing force, surface tension, and disjoining pressure, the undulations propagate in the form of a surface wave train. It is essential to understand how the surface waves evolve and propagate for the different applications to be successful.

In this paper, we theoretically and numerically study the axisymmetrical surface wave propagation phenomenon of a thin liquid film on a rotating or nonrotating disk under the lubrication condition. For liquid films on a rotating disk, the flow is driven by the centrifugal spinning. For liquid films on a nonrotating disk, the flow is driven by the external shearing force of an immiscible fluid blowing normal to the disk surface. We focus on the propagation of waves with long wavelength (surface tension effect is weak or negligible) and only briefly discuss the surface tension effect on the wave propagation. The effects of other important physical parameters such as the viscous force, centrifugal force, external shearing force and disjoining pressure are discussed in details. Interesting phenomena such as shock wave (hydraulic jump) formation and propagation, wave planarization (the reduction of wave undulation), and wave merging, are studied in detail.

II. THE FILM THICKNESS EVOLUTION EQUATION

Scarpulla *et al.*'s experiments show that the flow of molecularly thin liquid films on a solid surface can still be described by the continuum theory with the adoption of an enhanced effective viscosity [15]. As a result, we study our current problem from a continuum point of view. Under lubrication and axisymmetric conditions, when both gravity and Coriolis force are negligible due to a small film thickness and a small radial velocity, the radial momentum equation for the flow of a Newtonian liquid on a rotating disk reduces to

$$-\rho\omega^2 r + \frac{\partial p}{\partial r} = \mu\frac{\partial^2 u}{\partial z^2}, \tag{1}$$

where r is the radial coordinate, z is the coordinate normal to the disk surface, ω is the rotating speed of the disk, u is the radial velocity, p is the pressure, ρ is the density, and μ is the dynamic viscosity of the liquid, respectively (see Fig. 1) [14]. The lubrication assumption is valid when both Reynolds number of the flow $\mathrm{Re}=\rho u_{max}h_0^2/(\mu r_0)$ and slope of the film profile $\partial h/\partial r$ are much smaller than 1, where h_0 is the vertical length scale, r_0 is the horizontal length scale, and h is the film thickness, respectively. Under lubrication condition,
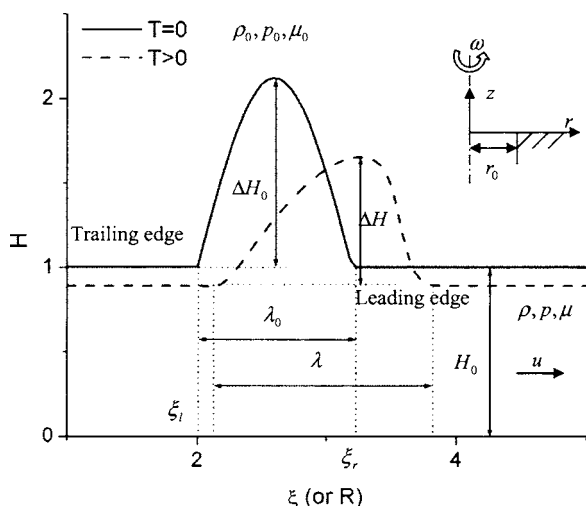
FIG. 1. The normalized initial geometry of a single hump superposed on a flat film and the evolved film profile at $T>0$. The initial hump is a half period of a sine function.

p is uniform across the film thickness, i.e., it does not depend on z. The radial velocity u is obtained by a direct integration of Eq. (1) in the z direction subject to a non-slip boundary condition at the disk surface

$$u|_{z=0} = 0, \tag{2a}$$

and a continuity of shear stress condition at the interface

$$\mu \frac{\partial u}{\partial z}\bigg|_{z=h} = A_* r, \tag{2b}$$

where $A_* = \omega^{3/2} \nu_0^{-1/2} \mu_0 / 2$ is a friction coefficient due to the shearing force imposed on the interface by the external flow induced by the rotating disk (for example, centrifugal pump flow of air or a different immiscible liquid) [6,16]. The film thickness h is a function of the radial coordinate r and time t. The kinematic and dynamic viscosities of the external fluid are denoted ν_0 and μ_0, respectively. The resulting velocity u from the integration is

$$u = \frac{1}{\mu}\left(-\rho\omega^2 r + \frac{\partial p}{\partial r}\right)\left(\frac{z^2}{2} - hz\right) + \frac{1}{\mu}A_* rz. \tag{3}$$

The volume flow rate per unit length of circumference q is calculated from the velocity distribution Eq. (3) as

$$q = \int_0^h u\, dz = \frac{1}{3\mu}\left(\rho\omega^2 r - \frac{\partial p}{\partial r}\right)h^3 + \frac{1}{2\mu}A_* r h^2. \tag{4}$$

Under axisymmetric condition, the mass balance equation for the liquid film can be written as

$$\frac{\partial h}{\partial t} + \frac{1}{r}\frac{\partial}{\partial r}(rq) = 0. \tag{5}$$

The evolution equation for the film thickness h is obtained by substituting Eq. (4) into Eq. (5) to yield

$$\frac{\partial h}{\partial t} + \frac{1}{6\mu}\frac{1}{r}\frac{\partial}{\partial r}\left[2\left(\rho\omega^2 r^2 - r\frac{\partial p}{\partial r}\right)h^3 + 3A_* r^2 h^2\right] = 0. \tag{6}$$

The pressure p within the film is obtained by a normal stress balance at the interface

$$p = p_0 - \Pi - \sigma\frac{1}{r}\frac{\partial}{\partial r}\left(r\frac{\partial h}{\partial r}\right), \tag{7}$$

where p_0 is the pressure of the external fluid (taken to be constant in this paper), σ is the surface tension coefficient, and $\Pi = A_3/h^3$ is the disjoining pressure due to van der Waals force (A_3 is the Hamaker constant and has a positive value for wetting liquids) [17]. Substituting Eq. (7) into Eq. (6) and normalizing it, we obtain the dimensionless governing equation for the film thickness

$$\frac{\partial(RH)}{\partial T} + \frac{\partial}{\partial R}\left\{R^2 H^3 + C_s R^2 H^2 - C_{dv}\frac{R}{H}\frac{\partial H}{\partial R}\right.$$
$$\left. + C_\sigma RH^3\frac{\partial}{\partial R}\left[\frac{1}{R}\frac{\partial}{\partial R}\left(R\frac{\partial H}{\partial R}\right)\right]\right\} = 0, \tag{8}$$

where $T = t\rho\omega^2 h_0^2/3\mu$, $R = r/r_0$, and $H(R,T) = h(r,t)/h_0$ are the dimensionless time, radial coordinate, film thickness, and external pressure, respectively. The horizontal length scale r_0 is chosen to be the radial coordinate of the inner boundary of the flow domain to be considered (see Fig. 1). The initial thickness h_0 of the flat part film is used as our vertical length scale. Equation (8) have three dimensionless groups. The dimensionless group $C_s = 3A_*/(2\rho\omega^2 h_0)$ represents the ratio between external shearing force and centrifugal force. Similarly, $C_{dv} = 3A_3/(\rho\omega^2 r_0^2 h_0^3)$ is the ratio of disjoining pressure force to centrifugal force and $C_\sigma = \sigma h_0/(\rho\omega^2 r_0^4)$ is the ratio of surface tension force to centrifugal force, respectively.

Equation (8) is a strongly nonlinear convection-diffusion type PDE and is numerically solved by an implicit finite volume method. The unsteady term is descretized by a first order backward time stepping method under a lump assumption. The centrifugal force, air shearing force, and disjoining pressure terms are descretized by a hybrid method in [18]. The surface tension term is descretized by the Crank-Nicolson method [19]. The linearized sparse matrix within each iteration is inverted by a preconditioned BiConjugate Gradient method [20]. At the two horizontal ends of the simulation domain, we apply the zero gradient boundary conditions.

III. THEORETICAL AND NUMERICAL RESULTS

From the definition of the dimensionless groups C_σ, C_s, and C_{dv}, we find that the flow can be divided into four regimes based on the film thickness when the radial length scale is fixed. In the first regime (regime A), the film thickness is relatively large and the surface tension effect is non-negligible. Centrifugal force is the dominant driving force for the wave propagation. The effects of external shearing and disjoining pressure are negligible, i.e., $C_\sigma \approx O(1)$, $C_s \ll 1$, and $C_{dv} \ll 1$. In the second regime (regime B), the film thickness is thin enough so that the surface tension effect
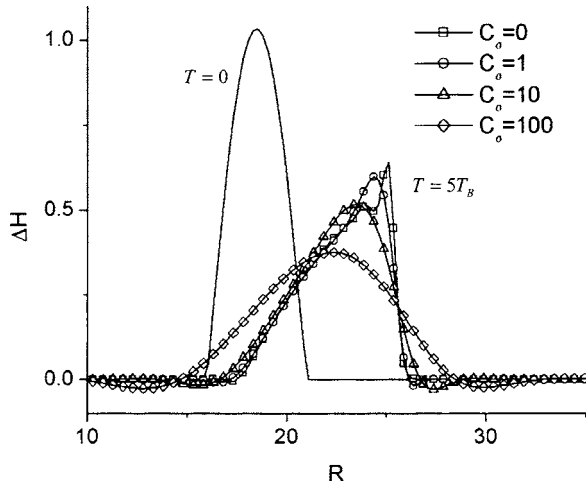
FIG. 2. The effect of surface tension on the wave propagation for a single hump wave driven by the centrifugal force with $C_s=0$, $C_{dv}=0$. [See Eq. (17b) for the definition of the breaking time T_B when $C_\sigma=0$.]
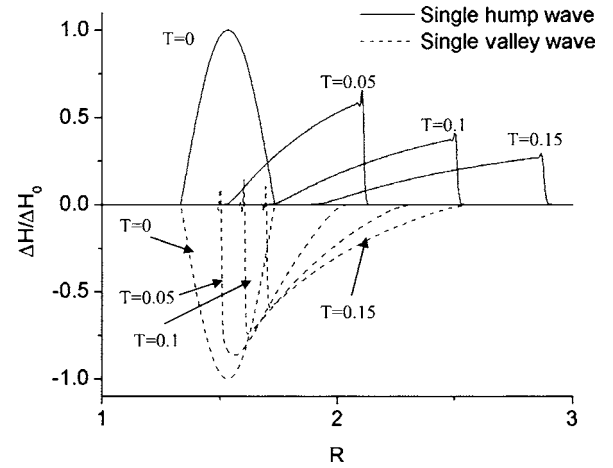

FIG. 3. Shock wave formation and propagation phenomenon for a single hump wave and a single valley wave driven by the centrifugal force with $C_s=0$, $C_{dv}=0$, and $C_\sigma=0$.

becomes negligible. Centrifugal force is the only dominant driving force for the wave propagation. Both external shearing and disjoining pressure effects are negligible, i.e., $C_\sigma \ll 1$, $C_s \ll 1$, and $C_{dv} \ll 1$. In the third regime (regime C), the film thickness is further reduced and the external shearing force becomes the dominant driving force. The centrifugal force, surface tension and disjoining pressure effects are negligible, i.e., $C_s \gg 1$ and $C_\sigma \ll 1$, $C_{dv} \ll 1$. In the fourth regime (regime D), the film becomes molecularly thin and the disjoining pressure effect becomes important. Both external shearing and disjoining pressure effects are dominant. The centrifugal force and surface tension effects are negligible, i.e., $C_s \gg 1$, $C_{dv} \sim O(1)$, and $C_\sigma \ll 1$. In between the four regimes are the transition regions.

A. Regime of flow with non-negligible surface tension effect

When the film thickness is relatively large, the centrifugal force and surface tension terms are dominant. The external shearing and disjoining pressure terms are negligible. Consequently, Eq. (8) simplifies into

$$\frac{\partial(RH)}{\partial T} + \frac{\partial}{\partial R}\left\{ R^2H^3 + C_\sigma RH^3 \frac{\partial}{\partial R}\left[\frac{1}{R}\frac{\partial}{\partial R}\left(R\frac{\partial H}{\partial R} \right) \right] \right\} = 0,$$
(9)

which is strongly nonlinear and cannot be solved analytically. Our numerical simulation shows that the surface wave is driven to migrate from the inner radial position to the outer radial position (see Fig. 2 for the case of a sine hump wave). The wave's magnitude is reduced and its wavelength is increased. Surface tension smears the wave and adds two dips (or over shoots) to the leading and trailing edges of a hump wave (or a valley wave). The surface tension smearing effect and the size of the dips (or over shoots) all increase with C_σ. Surface tension also slightly slows down the propagating speed of the wave peak. Nevertheless, when C_σ is reduced to below $O(1)$, the surface tension effect becomes negligible

and the wave steeps at the leading/trailing edge of a hump/valley wave. The wavefront eventually breaks and a shock wave (hydraulic jump) appears at the leading/trailing edge of a hump/valley wave as shown in Fig. 2 for a hump wave. The ripple after the shock wave for the curve corresponding to $C_\sigma=0$ in Fig. 2 is a numerical artifact. Similar numerical oscillations can be seen in Fig. 3.

After the formation of a shock, Eq. (9) breaks down locally within the shock region. Outside the thin shock region, Eq. (9) remains valid. As a result, Eq. (9) can be integrated to obtain useful information about the shock dynamics even after a shock is formed. Similar conclusion holds for the following regimes.

In our analysis, we assume all the dimensionless parameters including C_σ to be constant. When C_σ is not a constant (for example, due to the existence of a tangential temperature gradient along the interface), Sur and Bertozzi *et al.* found that undercompressive and reverse undercompressive shocks form for a draining film on a stationary plate driven by the surface tension gradient against gravity [21]. The shock wave formation phenomenon studied by Sur and Bertozzi *et al.* [21] is irrelevant to the shock wave formation phenomenon under the current study.

B. Regime of flow dominated by centrifugal force

When the centrifugal force term is dominant ($C_\sigma < 1$, $C_s \ll 1$, and $C_{dv} \ll 1$), Eq. (8) simplifies into

$$\frac{\partial H}{\partial T} + 3H^2\frac{\partial H}{\partial X} + 2H^3 = 0,$$
(10)

with a coordinate transformation $X=\log(R)$ and the dropping of the surface tension, external shearing and disjoining pressure terms. Equation (10) is a damped wave equation and can be solved by the characteristic method. Let $\tilde{H}(\xi)=H(\xi,0)$ be the initial film thickness at the initial radial location ξ [the starting location of each characteristic curve, see Eq. (13) and Fig. 1]. Along the characteristic curve

$$\frac{dX}{dT} = 3H^2, \qquad (11)$$

Eq. (10) becomes

$$\frac{dH}{dT} + 2H^3 = 0,$$

which can be integrated once with the using of the initial condition $H(\xi,0)=\widetilde{H}(\xi)$ to yield

$$H = \widetilde{H}(\xi)/\sqrt{1 + 4T\widetilde{H}(\xi)^2}. \qquad (12)$$

After we obtain the film thickness at time T, the transformed coordinate X along each characteristic curve is determined by integrating Eq. (11) once with the using of the initial condition $X|_{t=0}=\log(\xi)$ to yield

$$X = \log(\xi) + \tfrac{3}{4}\log[1 + 4\widetilde{H}(\xi)^2 T],$$

from which we obtain the original radial coordinate

$$R = \xi[1 + 4\widetilde{H}(\xi)^2 T]^{3/4}. \qquad (13)$$

Along each characteristic curve Eq. (13), the film thickness is determined by Eq. (12).

Under certain conditions, characteristic curves represented by Eq. (13) may intersect each other. When the intersection of characteristics occurs, H becomes multivalued and the wave breaks. The wave first breaks at $dR/d\xi=0$, or $4\widetilde{H}^2(\xi)T + 6\xi\widetilde{H}(\xi)\widetilde{H}'(\xi)T + 1 = 0$ from Eq. (13). A prime in this paper denotes a differentiation of the variable, for example, $\widetilde{H}'(\xi) = d\widetilde{H}(\xi)/d\xi$. The corresponding breaking time is

$$T_B = -\frac{1}{\widetilde{H}(\xi_B)[4\widetilde{H}(\xi_B) + 6\xi_B\widetilde{H}'(\xi_B)]}, \qquad (14a)$$

which is at its minimum when $\xi=\xi_B$. Since we always have $T>0$ and $\widetilde{H}(\xi)>0$, the breaking condition becomes

$$2\widetilde{H}(\xi) + 3\xi\widetilde{H}'(\xi) < 0. \qquad (14b)$$

As a result, if the initial film thickness profile has a large enough negative slope, the wave eventually breaks.

When the breaking condition Eq. (14b) is satisfied, from Eqs. (13) and (14a), we can exactly calculate the initial wave breaking location

$$R_B = \xi_B[1 + 4\widetilde{H}(\xi_B)^2 T_B]^{3/4} = \xi_B\left(\frac{3\widetilde{H}'(\xi_B)\xi_B}{2\widetilde{H}(\xi_B) + 3\widetilde{H}'(\xi_B)\xi_B}\right)^{3/4}. \qquad (15)$$

The appearance of multiple values for H (the breaking of the wave) corresponds to the formation of a shock wave (hydraulic jump). To understand the shock formation and propagation dynamics, we study the evolution of a single sine hump wave (with a plus sign) or a single valley wave (with a minus sign) superposed on a flat film (see Fig. 1 for the hump wave):
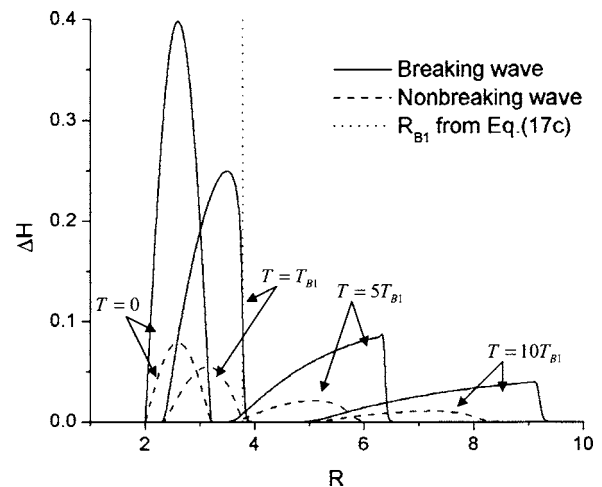

FIG. 4. Breaking sine hump wave (solid line) when the breaking condition is satisfied $[\Delta H_0 = 5\Delta H_B$, see Eq. (17a)] and nonbreaking sine hump wave (dashed line) when the breaking condition is slightly not satisfied ($\Delta H_0 = 0.99\Delta H_B$) with $C_s=0$, $C_{dv}=0$, and $C_\sigma=0$. The dotted line indicates the wave breaking location R_{B1} predicted by Eq. (17c) for the breaking hump wave.

$$H(\xi,0) = \begin{cases} 1, & \xi < \xi_l \\ 1 \pm \Delta H_0 \sin\left(\dfrac{\xi - \xi_l}{\lambda_0}\pi\right), & \xi_l \leqslant \xi \leqslant \xi_l + \lambda_0 \\ 1, & \xi_l + \lambda_0 < \xi, \end{cases} \qquad (16)$$

where ΔH_0 is the initial wave magnitude, λ_0 is the initial wavelength, and ξ_l is the initial radial coordinate of the trailing edge of the wave, respectively. The breaking condition [Eq. (14b)] for the hump described by Eq. (16) becomes

$$\Delta H_0 \geqslant \Delta H_B = \frac{2}{3\pi}\frac{\lambda_0}{\xi_l + \lambda_0}, \qquad (17a)$$

where ΔH_B is the required minimum hump height for the hump wave to break. The wave first breaks at the hump's leading edge ($\xi_B = \xi_l + \lambda_0$) at time

$$T_B = \frac{\lambda_0}{6\pi\Delta H_0(\xi_l + \lambda_0) - 4\lambda_0}, \qquad (17b)$$

and at the radial location

$$R_B = (\xi_l + \lambda_0)\left[\frac{3\pi\Delta H_0(\xi_l + \lambda_0)}{3\pi\Delta H_0(\xi_l + \lambda_0) - 2\lambda_0}\right]^{3/4}. \qquad (17c)$$

Our full numerical solution of Eq. (8) clearly demonstrates the formation of shock waves at the leading edge of a hump and at the trailing edge of a valley when the breaking condition is satisfied (see Fig. 3). Needham and Merkin's results also indicated the formation of shock wave driven by the centrifugal force for a different flow problem [22].

Figure 4 shows that the sine hump wave (solid line) described by Eq. (16) breaks when the breaking condition is satisfied $[\Delta H_0 = 5\Delta H_B$, see Eq. (17a)] and the wave does not break (dashed line) when the breaking condition is slightly
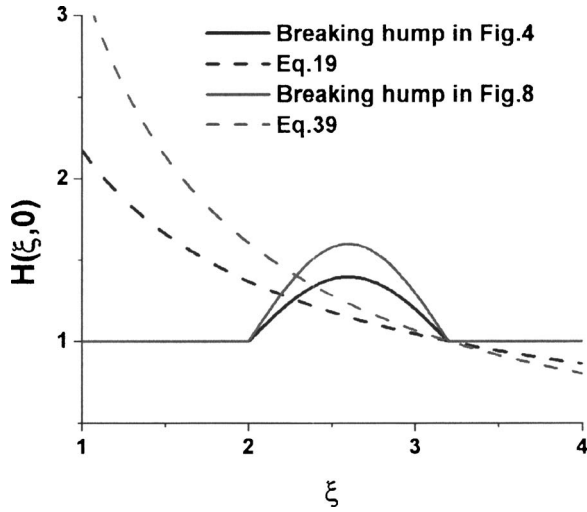
FIG. 5. Initial hump wave profiles and profiles predicted by Eqs. (19) and (39) that marginally satisfy the breaking conditions ($T_B = \infty$) for flow in regimes A and B.

not satisfied ($\Delta H_0 = 0.99 \Delta H_B$). The dotted line indicates the wave breaking location R_{B1} predicted by Eq. (17c) for the breaking hump wave. Figure 4 demonstrates that our theoretical prediction of the wave breaking conditions agrees very well with our full numerical simulation results.

From Eqs. (14a) and (14b), we know that a wave with an initial profile marginally satisfying the breaking condition

$$2\widetilde{H}(\xi) + 3\xi\widetilde{H}'(\xi) = 0, \tag{18}$$

breaks at time $T_B = \infty$. Equation (18) can be integrated once to yield

$$\widetilde{H}(\xi) = \beta_1 \xi^{-2/3}, \tag{19}$$

where β_1 is an integration constant. Equation (19) represents a group of curves corresponding to different values of β_1 and can be used to judge whether a wave will break or not. Waves that everywhere have a smaller negative slope than that of the curve represented by Eq. (19) at their crossing point do not break. Otherwise, the waves eventually break. Figure 5 plots both the initial profile for the breaking hump wave shown in Fig. 4 and the curve represented by Eq. (19) that crosses the hump at its leading edge. Because the hump has a larger negative slope than that of the curve represented by Eq. (19) at the leading edge, the hump wave breaks as shown in Fig. 4.

C. Regime of flow dominated by external shearing force

When the external shearing force is dominant and the effects of centrifugal force, surface tension and disjoining pressure are negligible, i.e., $C_s \gg 1$ and $C_\sigma \ll 1$, $C_{dv} \ll 1$, Eq. (8) can be further simplified and transformed into
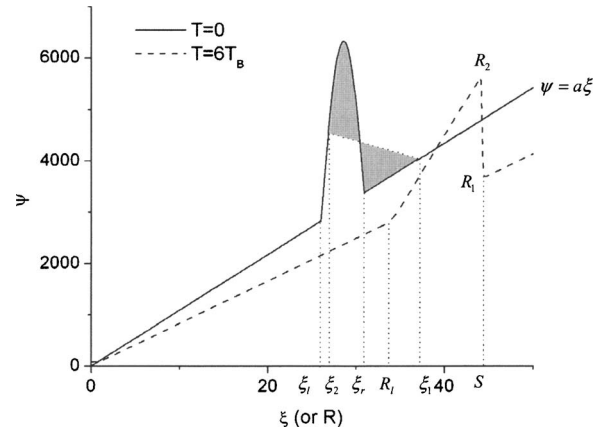

FIG. 6. The diagram of shock fitting method for flow in regime C. The dashed curve shows the formation of a shock at time $T = 6T_B$ [see Eq. (37b) for the definition of T_B for a sine hump wave].

$$\frac{\partial \psi}{\partial T} + \psi\frac{\partial \psi}{\partial R} = 0, \tag{20}$$

after we define a new variable $\psi = 2C_s RH$. Equation (20) is a nonlinear wave equation and can be solved by the characteristic method. Along a characteristic curve

$$R = \xi + F(\xi)T, \tag{21}$$

we have

$$\psi = F(\xi), \tag{22}$$

which is a constant. The variable $F(\xi) = 2C_s \xi \widetilde{H}(\xi)$ is the initial value of ψ at the starting location ξ of each characteristic curve. The wave breaking condition is

$$F'(\xi) = 2C_s[\widetilde{H}(\xi) + \xi\widetilde{H}'(\xi)] < 0, \tag{23a}$$

and the breaking time is

$$T_B = -1/F'(\xi_B), \tag{23b}$$

which is at its minimum when $\xi = \xi_B$. The wave eventually breaks if the initial $F(\xi)$ profile has a negative slope (see Fig. 6).

When the breaking condition Eq. (23a) is satisfied, from Eqs. (21) and (23b) we can exactly calculate the initial wave breaking location

$$R_B = \frac{\xi_B{}^2 \widetilde{H}'(\xi_B)}{\widetilde{H}(\xi_B) + \xi_B\widetilde{H}'(\xi_B)}. \tag{24}$$

We use the propagation of a single hump wave superposed on a flat film (see Figs. 1 and 6) as an example to illustrate the detailed shock formation and propagation dynamics in the current regime. In the region where characteristic curves intersect, ψ has multiple values. The multivalued region for ψ is replaced by a shock through an equal area rule [23]

$$\int_{\xi_2}^{\xi_1} F(\xi)d\xi = \frac{1}{2}[F(\xi_1) + F(\xi_2)](\xi_1 - \xi_2), \qquad (25)$$

where ξ_1 and ξ_2 are the initial radial coordinates of the ends of a chord, which eventually becomes vertical so that its ends becomes the ends of a shock at a later time T. The two ends of the chord evolve along their characteristic curves $R_1 = \xi_1 + F(\xi_1)T$ and $R_2 = \xi_2 + F(\xi_2)$ separately. When the chord becomes vertical, both R_1 and R_2 are equal to the shock location S (see Fig. 6). The equal area rule requires the two shaded areas in Fig. 6 to be equal to each other for the two ends R_1 and R_2 to form the ends of a shock at a later time. When $T \to \infty$, we have $\xi_1 > \xi_r$ and $\xi_2 \to \xi_l$. ξ_l and ξ_r are the initial radial coordinates of the trailing and leading edges of the hump, respectively. Because ξ_1 is located on the flat portion of the film with an initial thickness H_0 ($\xi_1 > \xi_r$ and see Figs. 1 and 6), $F(\xi_1)$ lies on a line passing through the origin with a constant slope $a = 2C_s H_0$ (see Fig. 6). As a result, we have

$$F(\xi_1) = a\xi_1. \qquad (26)$$

Consequently, the equal area rule Eq. (25) becomes

$$A = \tfrac{1}{2}[F(\xi_2) - a\xi_2](\xi_1 - \xi_2), \qquad (27)$$

where $A = \int_{\xi_l}^{\xi_r}[F(\xi) - a\xi]d\xi$ is the initial area of the hump above the line $\psi = a\xi$ (see Fig. 6). At time T, from the characteristic curve we have the shock location

$$S = \xi_1 + F(\xi_1)T = \xi_2 + F(\xi_2)T, \qquad (28)$$

which leads to

$$\xi_1 = \frac{\xi_2 + F(\xi_2)}{1 + aT}, \qquad (29)$$

by using Eq. (26). Substituting Eq. (29) into the equal area rule Eq. (27), we obtain

$$F(\xi_2) = a\xi_2 + \sqrt{\frac{2A(1 + aT)}{T}}. \qquad (30)$$

When $T \to \infty$, we have

$$\xi_2 \to \xi_l. \qquad (31)$$

From Eqs. (26)–(31), we obtain the shock location at time T,

$$S = \xi_2 + F(\xi_2)T = (1 + aT)\xi_l + \sqrt{2AT(1 + aT)}, \quad (32a)$$

and the jump of ψ across the shock wave,

$$[\psi] = F(\xi_2) - F(\xi_1) = \sqrt{\frac{2A}{T(1 + aT)}}. $$

From the jump of ψ we can calculate the shock strength (see Fig. 1 for the definition of ΔH)

$$\Delta H = \frac{[\psi]}{2C_s S} = \frac{1}{2C_s S}\sqrt{\frac{2A}{T(1 + aT)}}. \qquad (32b)$$

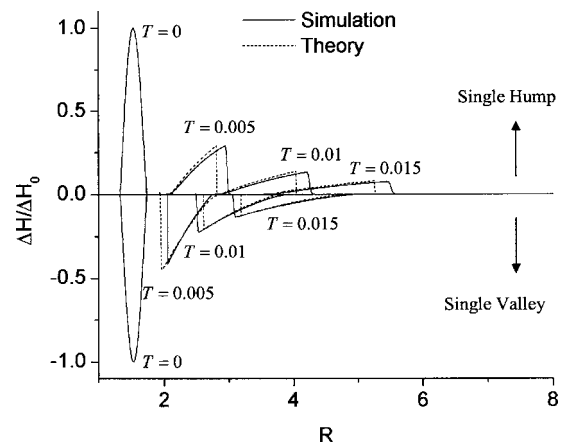The hump wavelength at time T becomes

FIG. 7. Shock wave formation and propagation phenomenon of a single hump wave (or a single valley wave) when the external shearing is dominant with $C_s = 54$, $C_{dv} = 0$, and $C_\sigma = 0$. The dashed line represents the theoretical results [Eqs. (32a)–(32c) and (35) for the hump wave and Eqs. (36a)–(36d) for the valley wave].

$$\lambda = S - R_l = S - \xi_l(1 + aT), \qquad (32c)$$

where $R_l = \xi_l + a\xi_l T$ is the coordinate of the trailing edge of the hump at time T.

To obtain the wave profile after the shock when $T \to \infty$, we expand $F(\xi)$ near ξ_l through a Taylor series expansion

$$F(\xi) = F(\xi_l) + (\xi - \xi_l)F'(\xi_l). \qquad (33)$$

Along the characteristic curve $R = \xi + F(\xi)T$, we have $\xi = R - F(\xi)T$, which is substituted into Eq. (33) to yield

$$\psi = 2C_s RH = F(\xi) = \frac{F(\xi_l) + (R - \xi_l)F'(\xi_l)}{1 + F'(\xi_l)T}. \qquad (34)$$

From the definition $F(\xi) = 2C_s \xi \tilde{H}$ and the relation $\tilde{H}(\xi_l) = H_0$, we obtain $F'(\xi_l) = 2C_s[H_0 + \xi_l \tilde{H}'(\xi_l)]$. Consequently, we obtain the hump's profile after the shock from Eq. (34)

$$H(R,T) = \frac{F(\xi)}{2C_s R} = \frac{H_0 + \xi_l \tilde{H}'(\xi_l) - \xi_l^2 \tilde{H}'(\xi_l)\dfrac{1}{R}}{1 + 2C_s T(H_0 + \xi_l \tilde{H}'(\xi_l))}. \qquad (35)$$

Equation (35) shows that the hump profile after the shock at time T is not a straight line. Outside the hump wave, the film remains flat and its decreasing film thickness is described by the result of Middleman [6] (see Figs. 1 and 7).

When a valley wave (the inverse of a hump wave) is superposed on a flat film, shock wave forms at the valley's trailing edge if the wave breaking condition Eq. (23a) is satisfied. At $T \to \infty$, by a similar shock fitting procedure, we obtain the valley's shock location, shock strength, wavelength and wave profile as
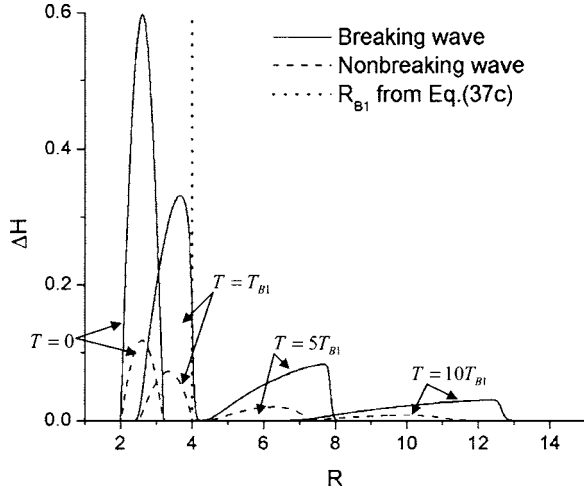
FIG. 8. Breaking sine hump wave (solid line) when the breaking condition is satisfied [$\Delta H_0 = 5\Delta H_B$, see Eq. (37a)] and nonbreaking sine hump wave (dashed line) when the breaking condition is slightly not satisfied ($\Delta H_0 = 0.99\Delta H_B$) with $C_s = 54$, $C_{dv} = 0$, and $C_\sigma = 0$. The dotted line indicates the wave breaking location R_{B1} predicted by Eq. (37c) for the breaking hump wave.

$$S(T) = (1 + aT)\xi_r - \sqrt{2AT(1 + aT)}, \tag{36a}$$

$$\Delta H = \frac{F(\xi_1) - F(\xi_2)}{2C_s S} = \frac{1}{2C_s S}\sqrt{\frac{2A}{T(1 + aT)}}, \tag{36b}$$

$$\lambda = (1 + aT)\xi_r - S, \tag{36c}$$

and

$$H(R,T) = \frac{-\xi_r^2 H'(\xi_r) + (H_0 + \xi_r H'(\xi_r))R}{(1 + 2C_s(H_0 + \xi_r H'(\xi_r))T)R}, \tag{36d}$$

where ξ_r is the initial radial coordinate of the leading edge of the valley wave.

When the external shearing is dominant, our theory and simulations show that shocks form at the leading edge of a hump wave and the trailing edge of a valley wave [described by Eq. (16)] when the breaking condition is satisfied (see Fig. 7). Figure 7 shows that our theoretical predictions of the shock properties and the wave profile after the shock [Eqs. (32a)–(32c), (35), and (36a)–(36d)] agree well with our full numerical solutions of Eq. (8) even at very small time T when $C_s = 54$, $C_{dv} = 0$, and $C_\sigma = 0$.

For the sine hump wave described by Eq. (16), the breaking condition (23a) becomes

$$\Delta H_0 \geqslant \Delta H_B = \frac{\lambda_0}{\pi(\xi_l + \lambda_0)}, \tag{37a}$$

where ΔH_B is the required minimum hump height for the wave to break at a later time. The wave first breaks at its leading edge ($\xi_B = \xi_r = \xi_l + \lambda_0$) at the breaking time

$$T_B = \frac{\lambda_0}{2C_s[\pi\Delta H_0(\xi_l + \lambda_0) - \lambda_0]}, \tag{37b}$$

and at the radial location

$$R_B = \frac{\pi\Delta H_0(\xi_l + \lambda_0)^2}{\pi\Delta H_0(\xi_l + \lambda_0) - \lambda_0}. \tag{37c}$$

Figure 8 shows that the sine hump wave (solid line) described by Eq. (16) breaks when the breaking condition is satisfied [$\Delta H_0 = 5\Delta H_B$, see Eq. (37a)] and the wave does not break (dashed line) when the breaking condition is slightly not satisfied ($\Delta H_0 = 0.99\Delta H_B$). The dotted line indicates the wave breaking location R_{B1} predicted by Eq. (37c) for the breaking hump wave. Figure 8 demonstrates that our theoretical prediction of the wave breaking conditions agrees well with our full numerical simulation results.

From Eqs. (23a) and (23b), we know that a wave with an initial profile marginally satisfying the breaking condition is

$$\widetilde{H}(\xi) + \xi\widetilde{H}'(\xi) = 0, \tag{38}$$

which breaks at time $T_B = \infty$. Equation (38) can be integrated once to yield

$$\widetilde{H}(\xi) = \frac{\beta_2}{\xi}, \tag{39}$$

where β_2 is an integration constant. Equation (39) represents a group of curves corresponding to different values of β_2 and can be used to judge whether a wave will break or not. Waves that everywhere have a smaller negative slope than that of the curve represented by Eq. (39) at their crossing point do not break. Otherwise, the waves eventually break. Figure 5 plots both the initial profile for the breaking hump wave shown in Fig. 8 and the curve represented by Eq. (39) that crosses the hump at its leading edge. Because the hump has a larger negative slope than that of the curve represented by Eq. (39) at the leading edge, the hump breaks as shown in Fig. 8. Nevertheless, the value of $F'(\xi)$ provides a more convenient way to judge whether a wave breaks or not. If $F'(\xi) < 0$ at certain location, the wave breaks. Otherwise the wave does not break.

We need to point out that all the results and conclusions for the current regime (IIIC) hold exactly if the disk is not rotating and the liquid film flow is driven by an immiscible external flow blowing normal to the disk surface under the condition that the external pressure, surface tension, and disjoining pressure effects are negligible. When an immiscible external flow blows normal to a disk (so called stagnation point flow [16,24]), the external shearing stress on the interface has a form similar to that of Eq. (2b). The surface tension has a similar effect on the wave propagation as in regime A.

D. Regime of flow dominated by external shearing force and disjoining pressure

When the film becomes molecularly thin, the disjoining pressure due to van del Waal's force becomes important. At the same time, the external shearing force is still dominant [$C_s \gg 1$, $C_{dv} \sim O(1)$, and $C_\sigma \ll 1$]. The centrifugal force and surface tension terms are negligible. Equation (8) simplifies into
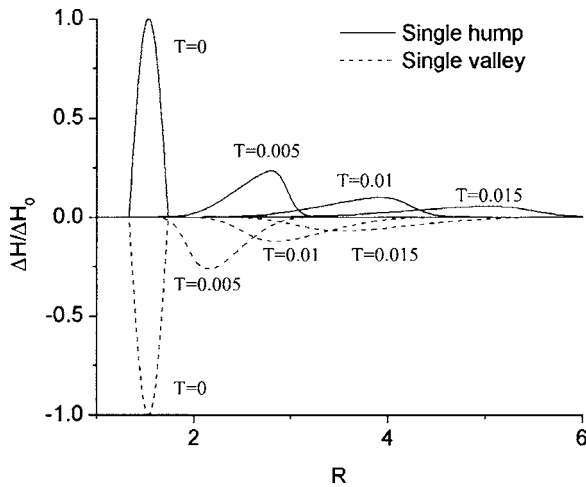
FIG. 9. Propagation of a single hump wave (or a single valley wave) when the disjoining pressure is nonnegligible with $C_s=54$, $C_{dv}=1.7$, and $C_\sigma=0$.

$$\frac{\partial(RH)}{\partial T} + \frac{\partial}{\partial R}\left(C_s R^2 H^2 - C_{dv}\frac{R}{H}\frac{\partial H}{\partial R}\right) = 0, \qquad (40)$$

which is difficult to solve analytically. The disjoining pressure term for a wetting film acts as a diffusion term and smears the shock as shown in our numerical results (Fig. 9).

Results in regime D also hold for the flow of liquid films driven by the external stagnation point flow on a nonrotating disk.

IV. DISCUSSION

Figure 10(a) plots the evolution of the shock location of a hump wave (Fig. 1) for the cases $C_\sigma=0$, $C_s=0$, $C_{dv}=0$ and $C_\sigma=0$, $C_s=54$, $C_{dv}=0$ and the location of hump's peak for the case $C_\sigma=0$, $C_s=54$, $C_{dv}=1.7$. Centrifugal force drives the shock (or peak) to migrate outwards slowly. The external shearing force greatly speeds up the outward propagation of the shock (or peak). Disjoining pressure slightly slows down the propagation. Figure 10(a) also shows that Eq. (32a) provides a good prediction of the peak location of the hump not only for flow in regime C $(C_s \gg 1, C_{dv} \ll 1)$ but also for flow in regime D $(C_s \gg 1, C_{dv} \approx O(1))$.

Figure 10(b) plots the evolution of the shock strength ΔH of a hump wave (Fig. 1) for the cases $C_\sigma=0$, $C_s=0$, $C_{dv}=0$ and $C_\sigma=0$, $C_s=54$, $C_{dv}=0$. For the purpose of comparison, we also plotted the evolution of ΔH (the relative height of the hump from the flat film surface) for the case $C_\sigma=0$, $C_s=54$, $C_{dv}=1.7$. Figure 10(b) indicates that centrifugal force, external shearing force and disjoining pressure all reduce the height of a hump wave (wave planarization). External shearing plays a dominant planarization role when the film thickness is thin enough. Figure 10(b) also shows that Eq. (32b) provides a good prediction of ΔH not only for flow in regime C $(C_s \gg 1, C_{dv} \ll 1)$ but also for flow in regime D $[C_s \gg 1, C_{dv} \approx O(1)]$.
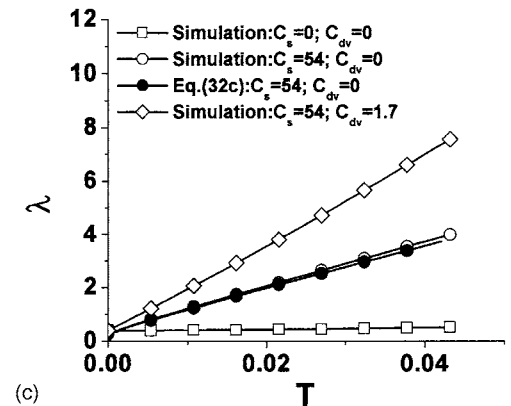
Centrifugal force, external shearing, and disjoining pressure all increase the hump's wavelength as shown in Fig.
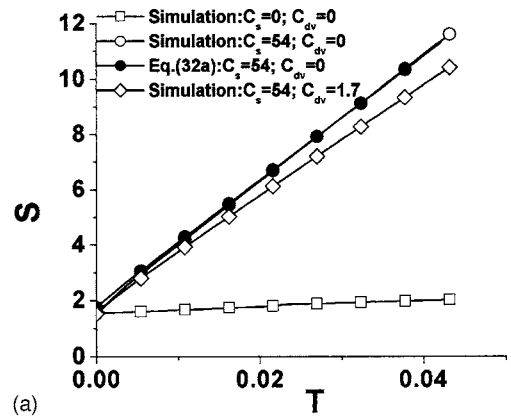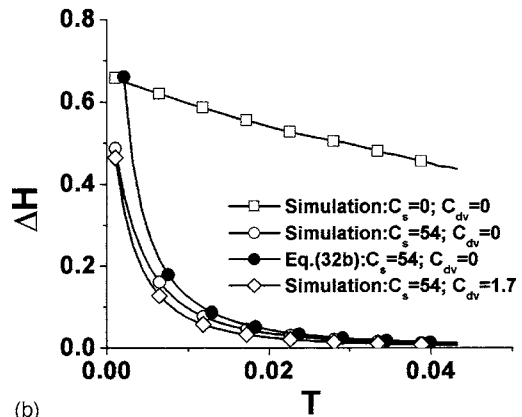
FIG. 10. Shock wave evolution of a single hump wave with $C_\sigma=0$: (a) Shock (or peak) location; (b) shock strength (or relative height); (c) Wavelength. The hump is cut off at 5% of its height in calculating the wavelength in the numerical simulation.

10(c). External shearing, and disjoining pressure have a dominant effect to increase the wavelength when the film is thin enough.

We have observations similar to Figs. 10(a)–10(c) for a single valley wave superposed on a flat film.

Another interesting phenomenon is the merging of waves induced by the disjoining pressure. The form of the final merged wave strongly depends on the overall volume of the wave train above the flat film. When the overall volume of a wave train above the flat film is positive, the wave train eventually merges into a single hump [see Fig. 11(a)]. When
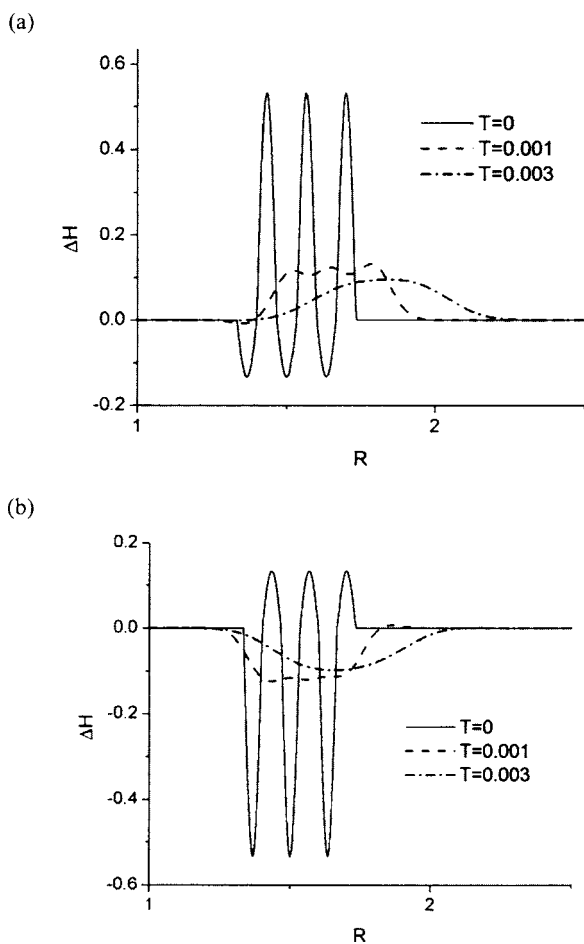
(a)

(b)

FIG. 11. The merging of a wave train into a single hump (a) or valley (b) when the initial overall volume of the wave train above the flat film is positive or negative: (a) the volume above the flat film is positive; (b) the volume above the flat film is negative (C_s =20, C_{dv}=1.7, C_σ=0).
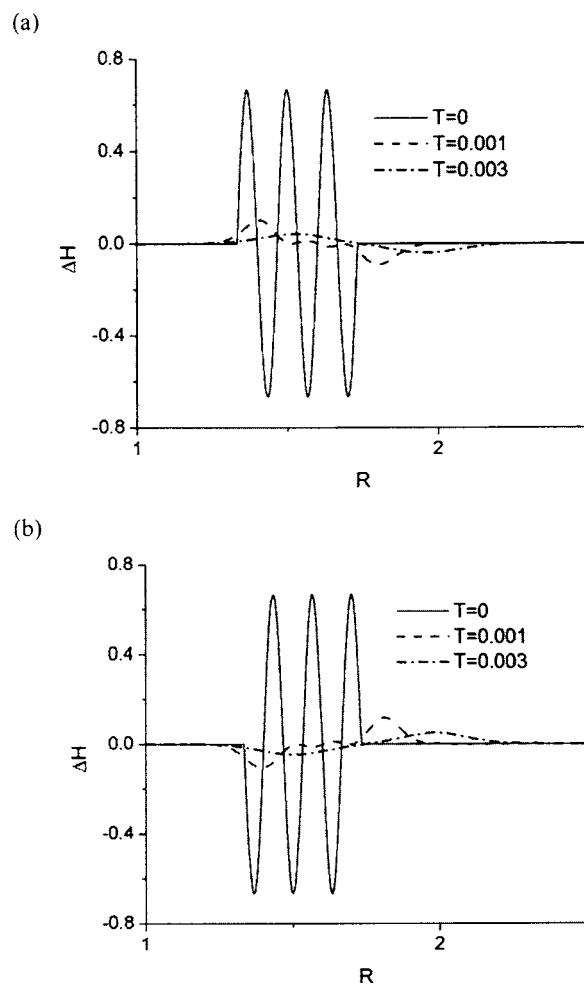
(a)

(b)

FIG. 12. The merging of a wave train into a single hump followed by a valley (a) or a single valley followed by a single hump (b) when the initial overall volume of the wave train above the flat film is zero: (a) the wave train is initially started with a hump and ended with a valley; (b) the wave train is initially started with a valley and ended with a hump. (C_s=20, C_{dv}=1.7, C_σ=0).

the overall volume of a wave train above the flat film is negative, the wave train merges into a single valley [see Fig. 11(b)]. When the overall volume of the wave train above the flat film is zero, the wave train merges into a single hump and a single valley with an equal amount of volume above or below the flat film. The single hump and valley do not merge afterwards (in theory it takes infinitely long time for them to merge, i.e., the wave train is totally planarized). The order of the single hump and single valley depends on how the wave train is started and ended. For the case shown in Fig. 12(a), the wave train merges into a single hump at the inner edge and a single valley at the outer edge. Figure 12(b) shows a reverse situation.

V. CONCLUSION

Surface wave propagation phenomena of a wetting liquid film above a rotating or non-rotating disk are studied numerically and theoretically. For films on a rotating disk, the surface wave evolution is driven by the centrifugal spinning.

For films on a nonrotating disk, the surface wave evolution is driven by the external shearing force induced by an immiscible flow blowing normal to the disk.

Our results show that the surface wave is driven to migrate outwards by the centrifugal and external shearing forces. The mobility of surface wave increases with the disk spinning speed and film thickness. Surface tension and disjoining pressure slow down the wave propagation. Shock wave may form and propagate driven by the centrifugal force and external shearing. Surface tension and disjoining pressure tend to smear the shock front. Multiple waves are merged by the disjoining pressure when the film becomes molecularly thin. Centrifugal force, surface tension, external shearing, and disjoining pressure, all planarize the surface wave by reducing its undulation and increasing its wavelength. When the film is thin enough, external shearing force and disjoining pressure dominate the wave planarization process.

[1] A. G. Emslie, F. T. Bonner, and L. G. Peck, J. Appl. Phys. **29**, 858 (1958).

[2] A. Acrivos, M. J. Shah, and E. E. Petersen, J. Appl. Phys. **31**, 963 (1960).

[3] W. W. Flack, D. S. Soong, A. T. Bell, and D. W. Hess, J. Appl. Phys. **56**, 1199 (1984).

[4] D. Meyerhofer, J. Appl. Phys. **49**, 3993 (1978).

[5] M. Yanagisawa, J. Appl. Phys. **61**, 1034 (1987).

[6] S. Middleman, J. Appl. Phys. **62**, 2530 (1987).

[7] T. J. Rehg and B. G. Higgins, Phys. Fluids **31**, 1360 (1988).

[8] L. E. Stillwagon and R. G. Larson, Phys. Fluids A **2**, 1937 (1990).

[9] L. E. Stillwagon and R. G. Larson, Phys. Fluids A **4**, 895 (1992).

[10] S. M. Troian, E. Herbolzheimer, S. A. Safran, and J. F. Joanny, Europhys. Lett. **10**, 25 (1989).

[11] N. Fraysse and G. M. Homsy, Phys. Fluids **6**, 1491 (1994).

[12] A. Oron, S. H. Davis, and S. G. Bankoff, Rev. Mod. Phys. **69**, 931 (1997).

[13] J. Gui, IEEE Trans. Magn. **39**, 716 (2003).

[14] J. S. Kim, S. Kim, and F. Ma, J. Appl. Phys. **73**, 422 (1993).

[15] M. A. Scarpulla, C. M. Mate, and M. D. Carter, J. Chem. Phys. **94**, 3368 (2003).

[16] M. Schlichting, *Boundary Layer Theory* (McGraw-Hill, New York, 1960).

[17] G. F. Teletzke, H. T. Davis, and L. E. Scriven, Rev. Phys. Appl. **23**, 989 (1988).

[18] S. V. Patankar, *Numerical Heat Transfer and Fluid Flow* (McGraw-Hill, New York, 1980).

[19] W. F. Ames, *Numerical Methods for Partial Differential Equations*, 2nd ed. (Academic, New York, 1977).

[20] W. H. Press, S. A. Teukolsky, W. T. Vetterling, and B. P. Flannery, *Numerical Recipes in Fortran 77* (Cambridge University Press, Cambridge, 1992).

[21] J. Sur, A. L. Bertozzi, and R. P. Behringer, Phys. Rev. Lett. **90**, 126105 (2003).

[22] D. J. Needham and J. H. Merkin, J. Fluid Mech. **184**, 357 (1987).

[23] G. B. Whitham, *Linear and Nonlinear Waves* (Wiley, New York, 1974).

[24] F. M. White, *Viscous Fluid Flow*, 2nd ed. (McGraw-Hill, New York, 1991).